ORIGINAL RESEARCH PAPER

The 2020 Mw 6.6 Vernadsky transform earthquake sequence: rupture and Coulomb stress changes surrounding an oceanic core complex

Guilherme W. S. de Melo[1] · **Neil C. Mitchell[2]** · **Sergey Y. Sokolov[3]**

Abstract

Oceanic core complexes (OCCs) are upwards-convex areas of outcropping lower crustal or upper mantle rocks raised to the seabed by normal faults, commonly associated with weak lithologies such as serpentinites. They are common adjacent to transform valleys of slow-spreading ridges. In this paper, we analyse the September 2020, Mw 6.6 strike-slip earthquake and its two-week long aftershock sequence within the Vernadsky transform valley, using recordings from regional seismic stations. The aftershocks occurred in two phases. During the first four days, ~131 events occurred east and northeast of the mainshock, overlapping an adjacent OCC complex along the northern flank of the transform valley. During the following nine days, 20 aftershocks occurred, including a Mw 5.8 event close to the OCC. To refine the locations of aftershocks, the spatial spread of the events (clustering) was refined by double-difference relocating 114 events, and five with teleseismic relative relocation. Modeling of static Coulomb stresses was carried out, based on a mainshock rupture length compatible with the 26–30 km horizontal extent of aftershocks. This revealed that the aftershocks occurred mainly in areas where static Coulomb stresses decreased, not increased. Other researchers have suggested that changes in fault strength can arise from dynamic stresses during major earthquakes, leading to seismicity in areas of decreased Coulomb stress. We explore this idea in the context of OCCs.

Introduction

Oceanic core complexes (OCCs) are sites at slow-spreading mid-ocean ridges (MORs) where deeper crustal and mantle rocks have been exposed at the seabed by large movements on normal faults, commonly leaving a corrugated seabed morphology (Cann et al. 1997; Blackman et al. 1998; Escartin et al. 2001, 2017; Smith et al. 2006, 2008, 2014). OCCs can contain rocks with weak minerals (e.g., serpentine and talc), suggesting a potential ability to slip with shallow dips when they were active (Blackman et al. 2002; Escartin et al. 2017). More

generally, serpentinite has been suggested to extend locally to 5 km depths (Minshull et al. 1998) or perhaps even to 15 km to explain aseismicity (Schlindwein and Schmid 2016). The presence of such weak minerals raises the question of whether stress changes around older (now generally inactive) OCCs can cause movements of their formative normal faults (reactivation), create new faults in lithosphere around them or lead to stress concentrations in the remaining unaltered lithosphere. If such effects occur more generally, they may, in turn, have implications for fluid circulation, the cooling of these local areas of oceanic crust, and crust and mantle alteration.

Hydroacoustic and seismic records of earthquakes have helped to reveal the pattern of deformation within active detachment faults, and temporal changes in epicentral locations have been related to cycles of stress accumulation and release (Collins et al. 2012; Parnell-Turner et al. 2017, 2021). As many OCCs have been identified in bathymetry adjacent to transform valleys, this prompts the question of how they and the lithosphere around them behave when within the influence of active transform-fault earthquakes.

✉ Guilherme W. S. de Melo
  gdemelo@geomar.de

[1] GEOMAR Helmholtz Centre for Ocean Research Kiel, Kiel, Germany

[2] Department of Earth and Environmental Sciences, University of Manchester, Manchester, UK

[3] Geological Institute, Russian Academy of Sciences, Moscow, Russia

Ⓐ Springer

Earthquakes of moment-magnitude Mw > 6.5 are common in the transform valleys of the equatorial Atlantic. For instance, the Romanche is a long strike-slip fault in which earthquakes of Mw > 7.0 occurred in 1994 (Abercrombie and Ekström 2001) and 2016 (Hicks et al. 2020). In such settings, the aftershock distribution and other seismological techniques show that oceanic strike-slip ruptures can extend over 60-100 km length (Hicks et al. 2020; Bao et al. 2022). Furthermore, seismic activity is commonly observed in Atlantic OCCs (Grevemeyer et al. 2013; Horning et al. 2017; Parnel-Turner et al. 2017, 2021). Strong earthquakes also cause stress changes in areas surrounding their epicenters that can trigger aftershocks. Modeling the changes in Coulomb stresses has been used to study some oceanic strike-slip and normal events to understand the temporal and spatial distribution of their aftershocks (Matias et al. 2007; Rollins and Stein 2010).

Here, we analyze the aftershock seismicity following a Mw 6.6 earthquake (September 6, 2020) within the Vernadsky fault segment of the Doldrums transform system using seismic records from regional stations (Fig. 1). The Mw 6.6 event lies within 5 km of a small ridge representing the active transform fault observable in multibeam sonar data.

We interpret this is the most likely site of the earthquake, thus constraining latitudinal uncertainty. Teleseismic relative relocations of five aftershocks recorded by global catalogs and double-difference relocation of most the aftershock sequence indicate that some of them may be related to an old OCC interpretable from multibeam data. We further explore, by modeling of Coulomb stress changes, how the Mw 6.6 and other transform earthquakes changed long-term stresses locally.

The 7.78˚N oceanic core complex in the Doldrums transform system

The Mid-Atlantic Ridge (MAR) 6.9-8.3ºN is offset longitudinally by 630 km over five fault segments of the Doldrums transform system (DTS, Fig. 2a). Those segments (Doldrums, Vernadsky, double Pushcharovsky, and Bogdanov) are separated by four intra-transform ridges (ITRs) ranging in length from 77 km (Bogdanov) to 229 km (double Pushcharovsky). Around 7.5˚N, the MAR has a spreading rate of 25–27 mm/year (DeMets et al. 2010), i.e., slow-spreading.
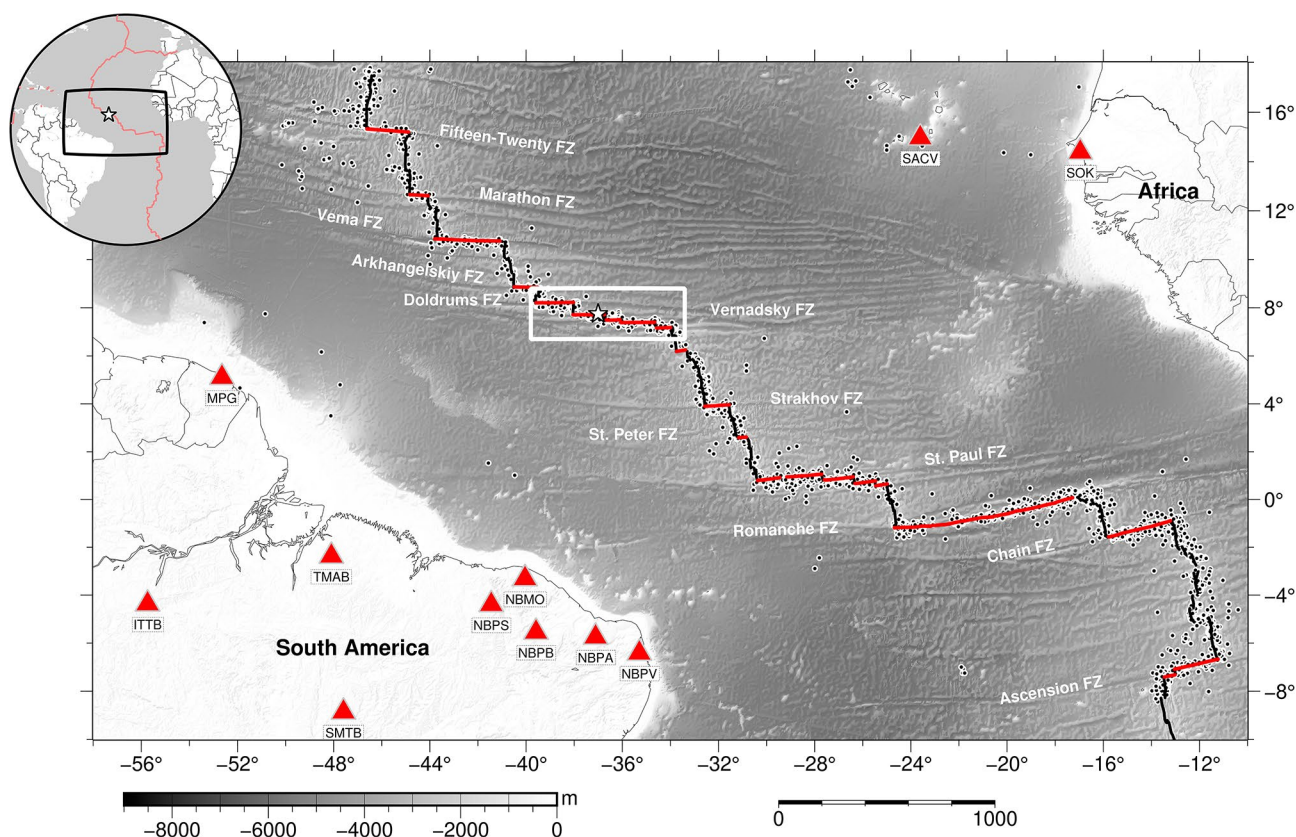

Fig. 1 Bathymetric map of equatorial Atlantic Ocean. Location of the Doldrums Transform System (white rectangle). Red triangles locates the land and or island seismic stations providing regional data for our study. White star shows the location of the 2020 Mw 6.6 Vernadsky earthquake. Black circles are epicenters from the International Seismological Centre (ISC) earthquake catalog. Transform faults derived from multibeam of Skolotnev et al. (2020) or bathymetric data of Ryan et al. (2009) are plotted in red line, with the black lines presenting the mid-ocean ridges from MAPRIDGES database (Sautter et al. 2024)
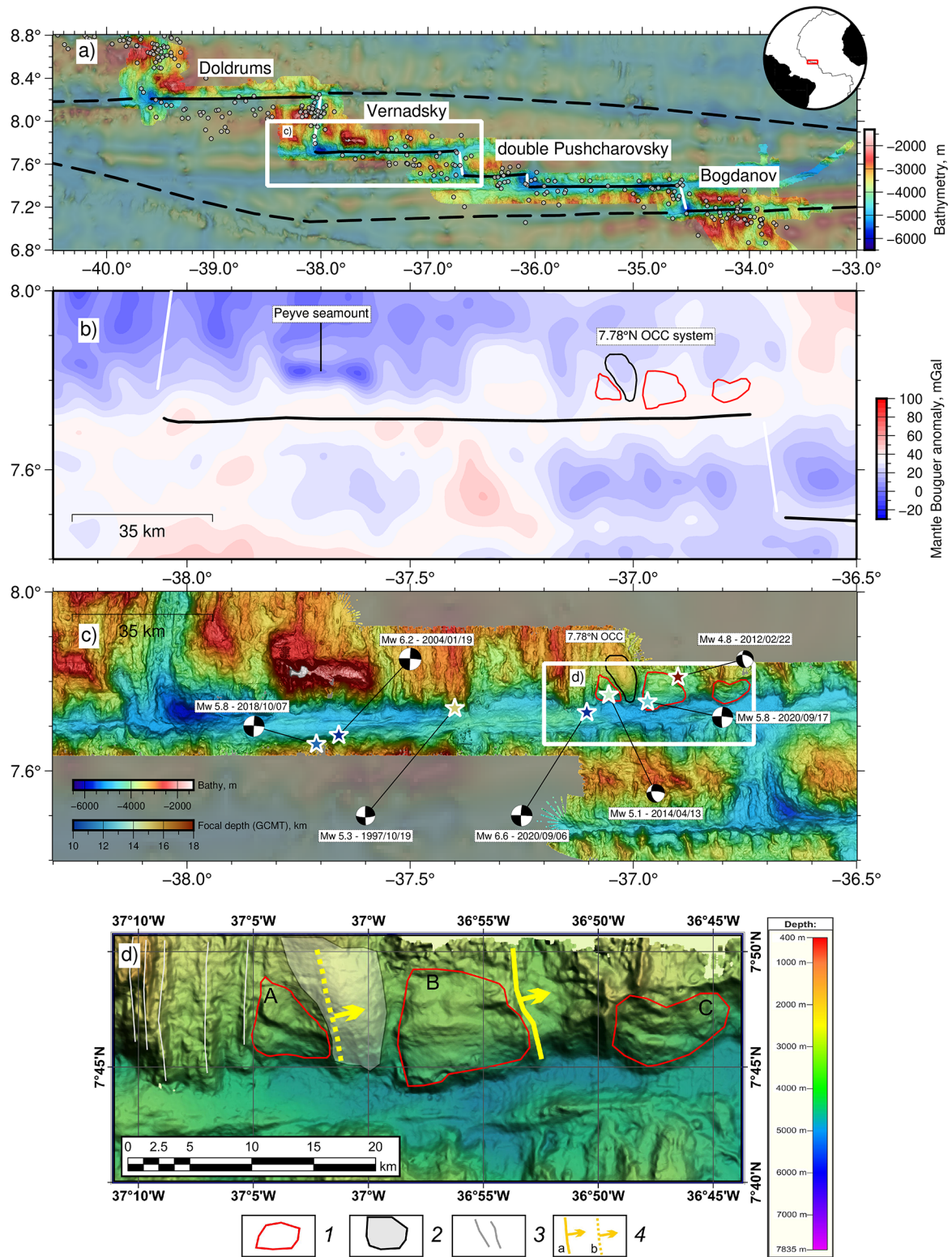
Fig. 2 **a**) Shaded relief map of the Doldrums transform system (DTS, dashed outline) derived from bathymetric data of Ryan et al. (2009) and swath multibeam data acquired by Skolotnev et al. (2020). Transform fault names are in white. Intra-transform ridges are marked by white lines. Gray circles are epicenters (ISC-EWH catalog). **b**) Mantle Bouguer anomalies calculated from the Sandwell et al. (2014) satellite-derived free-air anomaly grid. **c**) Enlarged bathymetry of the Vernadsky transform segment of the DTS. Stars denote historical earthquakes with associated focal mechanisms from the GCMT. White rectangle shows the area of (**d**). **d**) Bathymetry enlargement encompassing the 7.78ºN OCC. Key numbers: 1, outlines of the three suggested OCCs, 2, smooth ridge, 3, axis-parallel ridges, 4, high-angle normal faults (**a**, OCC breakaway, **b**, other). The normal fault forming the best developed OCC (segment B) would lie on its west side and dip downwards to the west

Multibeam data acquired during cruise 45 of R/V *Akademik Nikolaj Strakhov* in 2019 (Ivanova et al. 2020) revealed the existence of four OCCs within the active parts of the DTS (Skolotnev et al. 2020). The Vernadsky transform valley is ~145 km long west-east, 10–12 km wide, with a floor at 4700–4900 m depth below sea level (Fig. 2c), and with crustal ages 0-10 m.y. (Fig. S1; Seton et al. 2020). Focal mechanisms (Mw 4.8–6.6) based on the Global Centroid Moment Tensor (GCMT) catalog (Dziewonski et al. 1981; Ekström et al. 2012) indicate N-S left-lateral or E-W right-lateral strike-slip movements, and two oblique-slip normal movements. A narrow, southward-slanting east-west ridge lies within the floor of the transform valley from 37.1 to 37.6˚W, where it merges with the southern valley margin (Fig. 2c, d). Such ridges have typically been interpreted as caused by push-up by strike-slip motion (Searle 2013), and hence this feature likely overlies the principal transform displacement zone (PTDZ). N-S aligned ridge-and-valley morphology, orthogonal to the transform fault, is observed between 36.7˚ and 37.2ºW on the north flank of the Vernadsky transform valley (Fig. 2d). Following the geomorphology of OCCs observed elsewhere (Bonnemains et al. 2017), we interpret a region at ~7.78˚N with E-W lineations and upward-curved morphology at segment B in Fig. 2d as an OCC. If correct, the normal fault that created this surface would have lain on its west side (towards the modern ridge axis) and dips westward. Two further segments (A and C in Fig. 2d) also contain E-W trends, although these are more ambiguous OCCs, as they could alternatively represent hook faults (Searle et al. 1998) or landslides in the valley wall. A broad ridge ~8 km E-W and 20 km N-S separates A and B. Its smooth surface contrasts with the lower and more irregular valley relief between B and C, but both are interpreted as due to axial volcanism (Peyve et al. 2022). Age differences across the transform valley are ~8-9 m.y. at these OCC segments (Fig. S1).

Bouguer anomalies were computed assuming a uniform crustal thickness of 6 km with crustal and mantle densities of 2700 and 3300 kg/m^3 (Blackman et al. 2008; Searle 2013; Mallows and Searle 2012). A gravity anomaly of 0–20 mGal associated with the 7.78ºN OCC (Fig. 2b) implies thinner crust relative to the surrounding crust or localized higher density mantle.

Seismicity over the Vernadsky transform fault segment

We analyzed seismographic records of the Mw 6.6 Vernadsky earthquake (2020/09/06) and aftershocks from regional broad-band stations located at distances of 1200–2400 km. These seismic records were obtained from the Incorporated Research Institutions for Seismology Data Management Center (IRIS DMC) and the Brazilian Seismographic Network (RSBR, Bianchi et al. 2018). The NBPA, NBPV, NBPB, NBMO, NBPS and SACV were used for locating most earthquakes with magnitude < 4.5. The MPG and SOK data were used for magnitudes > 4.5 (better signal/noise ratio). Heliplots from NBMO station are shown in Figs. S2-S13. We used the HYPO71 plugin of the SCOLV program of the SeiscomP3 package (Lee and Valdes 1985; Hanka et al. 2010) to locate the aftershocks with a 1D velocity model based on CRUST1.0 (Table S1, Laske et al. 2013). After applying a Butterworth 3–6 Hz bandpass filter to the seismograms, the Pn phases were manually picked with estimated time uncertainties of ± 0.5s for events body-wave magnitudes (mb) < 4.0 and lower signal-to-noise ratio (Fig. 3). The procedure followed that used to relocate swarms at 4–5ºN on the Mid-Atlantic Ridge (de Melo et al. 2021).

The body-wave magnitudes (mb) range from 3.8 to 6.6, with most between 3.8 and 4.0 (Fig. 4a). The Mw 5.8 (GCMT) aftershock was represented by a weaker 5.6 magnitude on the mb scale (Table S2) (magnitudes commonly differ 0.1–0.6 units between mb and Mw scales in the equatorial Atlantic (Kim et al. 2024). Random uncertainties in epicenter location are 1–21 km decreasing with increasing magnitude (Fig. 4b; Table S2). Most uncertainties are < 11 km (Fig. 4c; Table S2). Figure 4d shows that ~90% of the earthquakes located have a root mean square (RMS) uncertainty of < 0.3s (Table S2). Total RMS range is 0.1–1.9 s.

The GCMT focal mechanisms (Ekström et al. 2012) suggest that both the mainshock (Mw 6.6) and largest aftershock (Mw 5.8) had strike-slip mechanisms (Fig. 5a). The different global catalogs show different locations, most likely reflecting different stations used, though with the Mw 6.6 mainshock locations nevertheless all inside the transform valley. Three epicenter locations for the Mw 6.6 event (Fig. 5a) lie within 5 km of the east-west ridge interpreted as the PTDZ. The focal mechanisms of two of them are consistent with right-lateral strike-slip movement on an E-W fault. The outlying GCMT event also has an EW strike slip mechanism. The ISC moment tensor solution suggests a compressional focal mechanism (Fig. 5a), though no information is available to explain the discrepancy with the other mechanisms. As reverse faulting is incompatible with the tectonic environment, the Mw 6.6 event is considered here most likely to be strike-slip.

Aftershock activity declined rapidly with time (Fig. 5b). Sixty-nine aftershocks occurred on the first day, with epicenters migrating eastward to the area with higher 8-9 m.y. crustal age difference (Fig. S1; Fig. 5e). Most of the epicenters were located within ~25 km of the mainshock, and south of the 7.78ºN segments (Fig. 5e). The daily numbers of
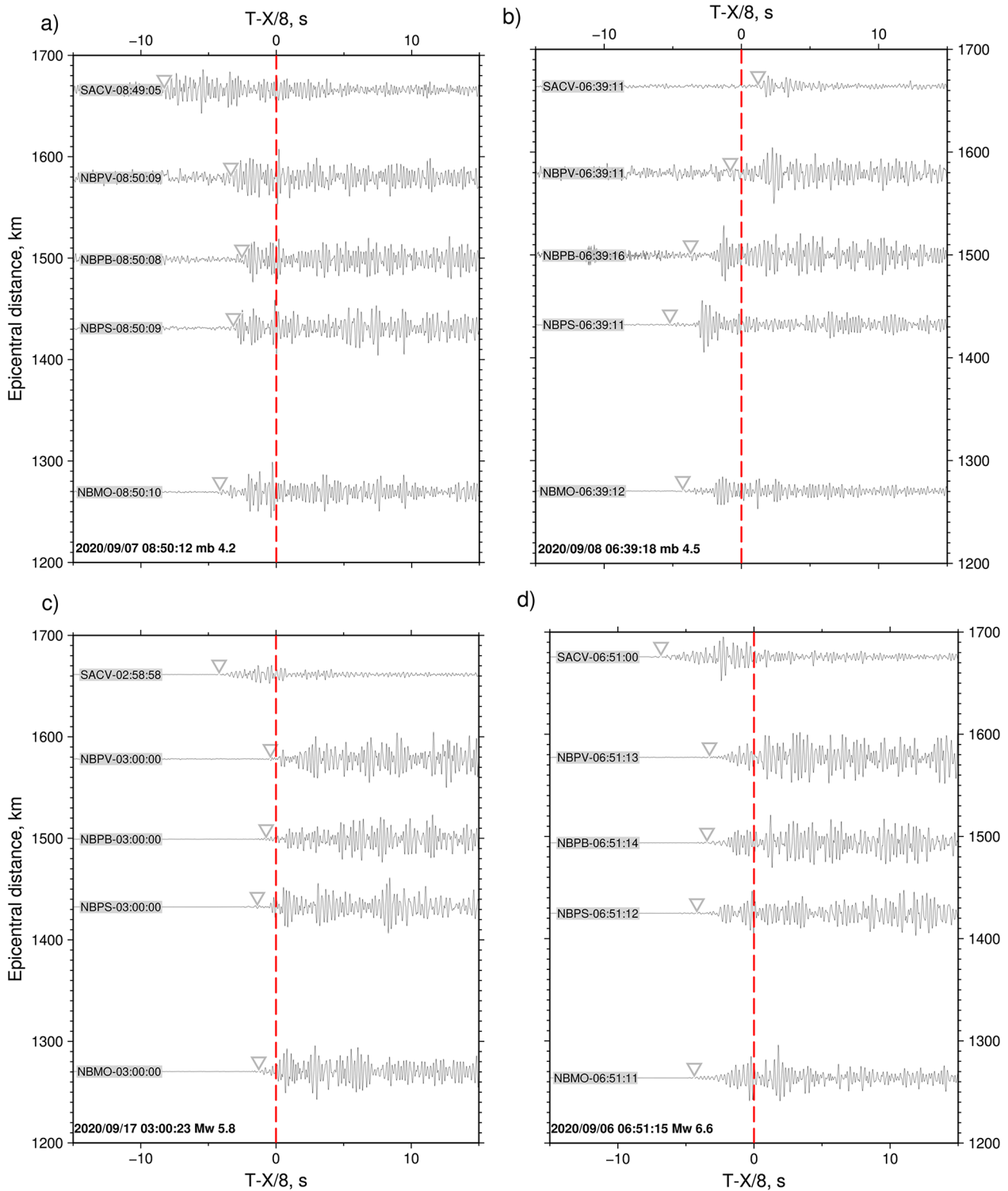
Fig. 3 Epicentral distance versus reduced travel time waveform examples (time reduced with a velocity of 8 km/s). Records have been referenced to the five main stations analyzed in this study after applying a 3–6 Hz Butterworth filter. Panels **a**) to **d**) are seismograms of events with magnitudes 4.2, 4.5, 5.8, and 6.6. Inverted triangles mark identifiable Pn arrivals
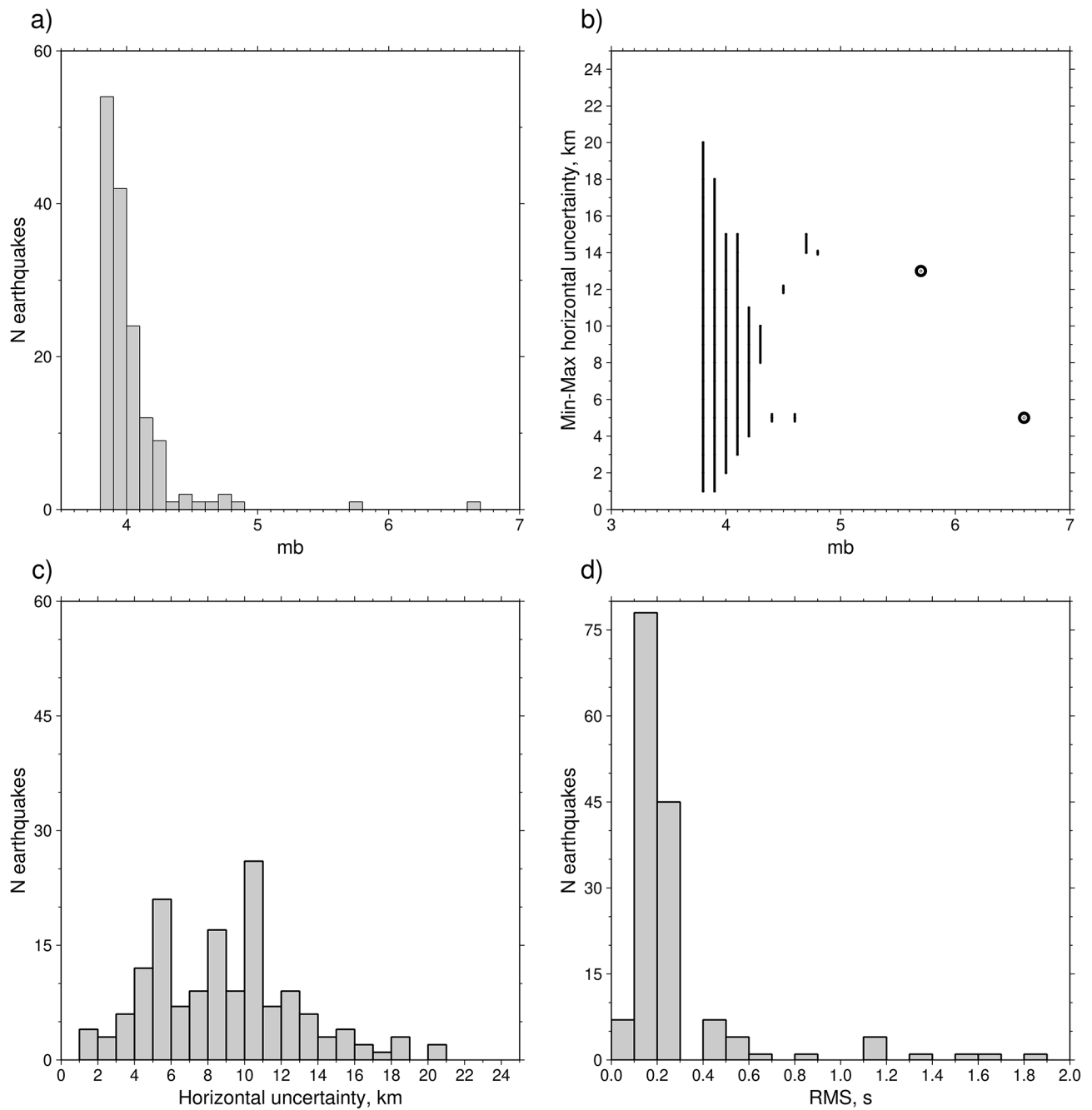
Fig. 4 a) Body-wave magnitude (mb) distribution of the full main-shock-aftershock sequence derived from the regional seismic recordings. **b**) Minimum-maximum horizontal uncertainty distribution of the data in (**a**). Bold circles highlight the Mw 6.6 and Mw 5.8 events. **c**) Distribution of horizontal uncertainties and **d**) root-mean square (RMS) distribution of located aftershock time uncertainties

earthquakes decreased to 39 (September 7), 16 (September 8) and 10 (September 9–11). The seismicity rate increased again with four events on September 13 (south of the OCC) and two on both September 14 and 15 (on the northern wall of the transform valley). On September 17, another six events were recorded, including the Mw 5.8 event. Our epicenter for the Mw 5.8 event is on the SW side of the OCC segment B with position uncertainties overlapping the

suggested normal fault that formed the OCC. On September 18 and 19 three events were located in the same area as September 17 (with estimated horizontal uncertainties of 8–15 km).

We relocated the earthquake catalog using the double-difference HYPODD software (Waldhauser and Ellsworth 2000). HYPODD has been used to relocate earthquakes from the differential arrival times of P and/or S waves at

Fig. 5 Distribution of the seismicity around the 7.78ºN oceanic core complex. **a**) Epicentral locations with focal mechanisms of different global catalogs for both the main Mw 6.6 event (red beach balls) and subsequent Mw 5.8 event (blue beach balls). Other annotation as Fig. 2d. **b,c**) Event frequency and magnitudes versus time (axes annotated in days of the month). Magnitudes were obtained from the HYPO71 results. d) Segment of Fig. 2d with 151 aftershock epicenters located using HYPO71. **e**) Those epicenters color-coded by date. Focal mechanisms are from the GCMT database, but shown at our new epicentral locations. Stars show epicenters of the 2020 Mw 6.6 and Mw 5.8 events relocated here. Circles locate historical GCMT events that suggest oblique-normal slip movements
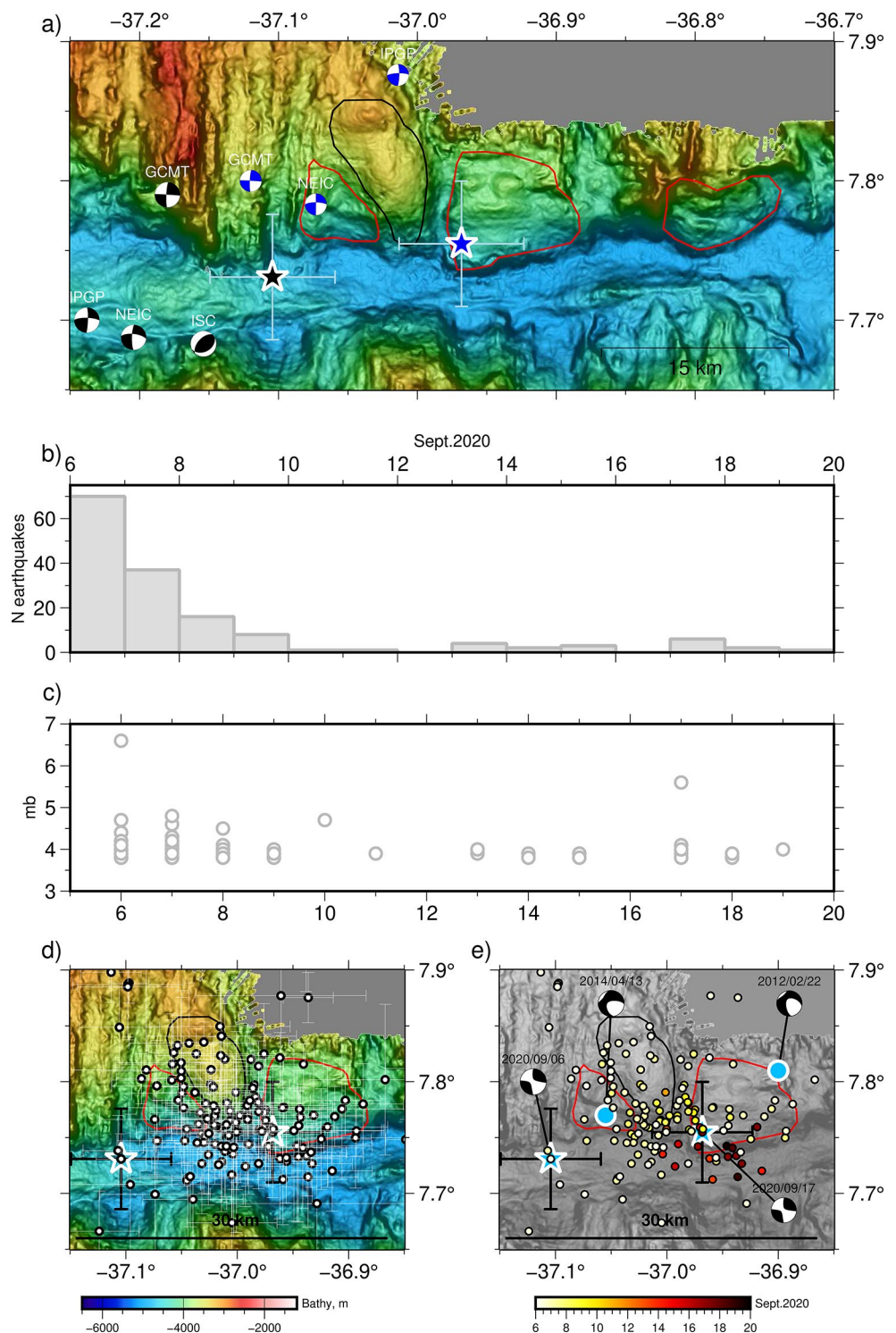
both local, regional, and teleseismic distances (Waldhauser and Schaff 2007). We mainly used the P-wave travel times obtained using HYPO71, with full weight, whereas S-waves, available for some events, were given half that weight. We tested different values of damping factors to adjust and maintain a stable inversion, until the initial damping factor values resulted in unstable inversions with large condition numbers (Waldhauser and Schaff 2007). We used the velocity model of Henig et al. (2012), previously used in the Atlantis Massif (Fig. 6a) to relocate the events.

A total of 114 events were relocated (Table S3) with uncertainties of 0.1–9.7 km (east-west) and 0.1–4.6 km (north-south). The other 36 earthquakes did not converge within the location constraints. The resulting epicenters

(Fig. 6c) are more spatially focused than those obtained initially with HYPO71 (Fig. 6b). The epicentral displacements from the inversion (Fig. 6d, e,f) are 1.94 km (east-west) and 2.13 km (north-south) (mean standard deviations).

Accuracy in epicenter relocation

The Mw 6.6 mainshock located using HYPO71 lies 4.8 km north of the PTDZ (Fig. 5a), which we suggest is the most likely site of the earthquake rupture. The latitude of this location is similar to the GCMT, IPGP, NEIC, and ISC epicenters. The proximity of our Mw 6.6 mainshock to the PTDZ suggests that the event is located well in latitude (i.e., the bias is only 4.8 km due to regional mantle velocity variations not represented in the Earth velocity model). Similarly, globally detected events recorded in local ocean bottom seismometer networks have also been found to coincide (Hicks et al. 2020; McGuire et al. 2012), suggesting that epicenter bias is modest. Considering the uncertainties after relocation with HypoDD (Fig. 6), along with the above
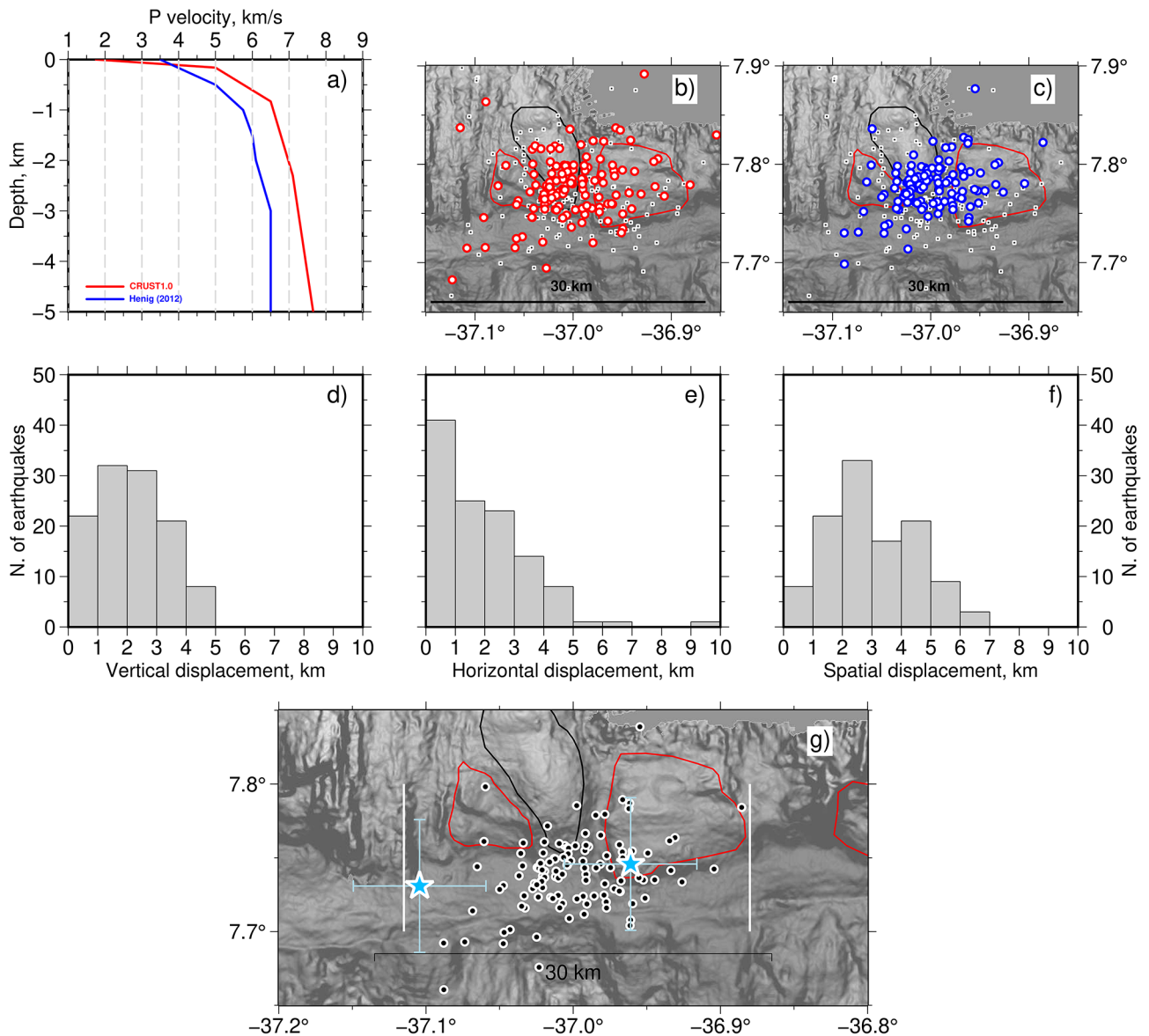

Fig. 6 Results of double-difference relocations of aftershock seismicity using the HypoDD package. **a)** Velocity profiles of the CRUST1.0 and Henig et al. (2012) models used in the relocations. **b,c)** Relatively relocated epicenters using the CRUST1.0 and Henig (2012) models, respectively (colored circles).White squares show the epicenters initially located using HYPO71 with CRUST1.0. **d)** to **f)** distribution of vertical, horizontal, and spatial epicenter displacements following relative relocation (using the Henig (2012) velocities). **g)** Final epicenters after applying a 4.8 km southward shift in latitude of the HypoDD catalog to account for the bias in the Mw 6.6 epicenter interpreted to have ruptured the PTDZ (the Mw 6.6 location is shown without this southward correction). White line shows the approximate extent of epicenters

🠂 Springer

4.8-km proximity of the Mw 6.6 event to the PTDZ, most of the relocated aftershock epicenters are confined mainly to the south side of the OCC segments. If the 4.8-km separation of Mw 6.6 event from the PTDZ represents a general bias, the aftershocks in Fig. 6c lay 4.8 km south of where shown. The event locations adjusted for this bias are shown in Fig. 6g. Therefore, the aftershocks lay within the transform valley floor and wall, including the OCC segment B.

Waldhauser and Schaff (2007) argued that epicenters of double-difference relocations can differ by more than 10 km from locations obtained from global recordings in the International Seismological Centre (ISC) catalog. Cleveland et al. (2018) also observed that relocated epicenters from regional recordings can differ by up to 11 km, even after using surface waves (earthquake magnitudes 4–6). Relocations of smaller earthquakes should be larger (Pan and Dziewonski 2005). Our suggested 4.8 km bias in HypoDD relocated epicenters is compatible with the uncertainties found in these other studies.

Surface wave relative relocation of the aftershocks of mb > 4.5

Five aftershocks with mb>4.5 (GCMT Mw > 4.9), including the Mw 5.8 event, have been recorded by stations at teleseismic distance and included in the GCMT catalog. These were: Sept.7 11:03:20 Mw 5.1; Sept.7 21:19:05 Mw 4.9; Sept.7 21:22:46 Mw 4.9; Sept.10 22:26:40 Mw 5.0; Sept.17 03:00:23 Mw 5.8. We used the epicenter and origin times obtained with HYPO71 as the initial parameters for relative relocation. The relative relocation procedure (McGuire 2008) relocated the five earthquakes using teleseismic records of surface waves. The procedure uses the difference in surface-wave travel time from the cross-correlation between two events to obtain the new relative position of the second event, using the coordinates of the first event as a reference (master). Before running the procedure, the surface wave records were bandpass filtered (0.02–0.04 Hz). The methodology assumes that the two paired earthquakes have similar focal mechanisms. Other similar procedures have been applied to investigate epicenter of oceanic seismicity using teleseismic records (Howe et al. 2019; Cleveland et al. 2018). We analyzed only those earthquakes with good teleseismic records and teleseismic station coverage (Fig. 7), using the HYPO71-derived epicenter of the Mw 6.6 earthquake as the master.

In the results (Fig. 7, Table 1), two events being the Sept. 7 Mw 5.1 (Fig. 7) and Sept.10 Mw (Fig. S14; Fig. 7) were relocated to east close to the Mw 6.6 mainshock, with separaton distance of 1.6±2.9 and 3.8±1.7 km away from the mainshock. These two events may have occurred on or near the rupture of the mainshock at PTDZ. However, the two Sept.7 earthquakes with Mw 4.9 (Figs. S15, S16; Fig. 7), and Sept.

17 Mw 5.8 (Fig. S17; Fig. 7), were relocated to the north walls of the transform valley, with separation distance of 14.2±1.5, 14.5±1.5, and 8.2±1.2 km away of the mainshock. These three aftershocks were relocated to the smooth surface ridge, with the easterly of them near the edge of the OCC (segment B), where we suggest the normal fault that formed the OCC lies.

Focal depths of the Mw 6.6 mainshock and Mw 5.8 aftershock

Analysis of recordings from ocean bottom seismometers over active OCCs elsewhere have located seismic activity 3–12 km below seafloor (Craig and Parnell-Turner 2017). For a better constraint of seismicity in our case, we modeled surface waveforms using the ISOLA package (Sokos and Zahradnik 2008; Zahradník and Sokos 2018) to derive the earthquake hypocenters for the Mw 6.6 and 5.8 events. The procedure (de Melo et al. 2021) used data from six stations (ITTB, NBMO, MPG, SOK, SACV, SMTB) at 1100–2900 km distance (Fig. 1; Fig. 8). The data were also those obtained from the IRIS DMC and RSBR. Prior to the inversion, the data was corrected for instrumental response and bandpass filtered (0.02–0.04 Hz). Two Brazilian land stations exhibited higher signal-to-noise ratio (0.01–0.03 Hz). The strike/dip/rake angles and location from the GCMT catalog (Dziewoński et al. 1981; Ekström et al. 2012) were fixed, so that only hypocentral depth was varied. A 1D velocity model from CRUST1.0 (Laske et al. 2013) was used.

The Mw 6.6 event was first modeled using the surface waveform approach. Its epicenter was located at 7.79ºN, 37.18ºW. The 5.8 Mw event was subsequently located further northeast at 7.80ºN, 37.14ºW near the B section of the 7.78º OCC. Based on the the GCMT database, strike-slip focal mechanisms with nodal planes of 273°/89°/-173° were observed for the Mw 6.6 event and 274°/86°/-171° for the Mw 5.8 event.

For the Mw 6.6 mainshock, the best-fitting waveforms suggest a hypocenter at 6+/-2 km depth below seafloor and centroid time + 1.2 s (Fig. 8; Table 2). For the Mw 5.8 aftershock, the best-fit hypocenter lies at 8+/-2 km depth and centroid time at + 0.4 s (Fig. S18; Table 2). The variance reductions of the correlation between observed and synthetic waveforms were 0.41 and 0.52 for the two earthquakes, respectively, with condition numbers (CN) of 7.7 and 9.0 (good inversions have CN < 10 (Sokos and Zahradnik 2008). In the GCMT inversions, the sea water layer is ignored (Ekström et al. 2012). Ekström et al. (2012) argued that the GCMT inversion is unstable for shallow oceanic earthquakes, hence they are mostly fixed at 12–13 km depth. Our modeled hypocenters are 6.0 and 10.3 km, shallower than the GCMT solutions, but as expected considering the local 4.2 km water depth (de Melo et al. 2021, 2024a).

Fig. 7 Relative relocation from surface wave cross-correlation. Upper side: Global distribution of the seismic stations used in analysis, and map with the changes in location of five events of magnitude>4.9 in the GCMT catalogue with relative relocation (no 4.8-km bias correction has been applied). Blue squares: epicenters located using HYPO71, red circles: the teleseismic relatively relocated epicenters. Blue star locates the epicenter of the mainshock used as the master (original location with HYPO71). Bottom side: Waveforms from the mainshock Mw 6.6 (shown in blue) are crosscorrelated with seismograms from the time of the Sept. 7 at 11:03, Mw 5.1 (shown in red). The relative location is defined using the differential arrival times (bottom panel, blue circles), which are fitted using a grid search to minimize the L1 norm (black line and red dots). In this case, the new location of the Mw 5.1 event occurred at coordinates 7.7311 latitude and -37.1185, which locates 1.6+/-2.9 km away from the mainshock
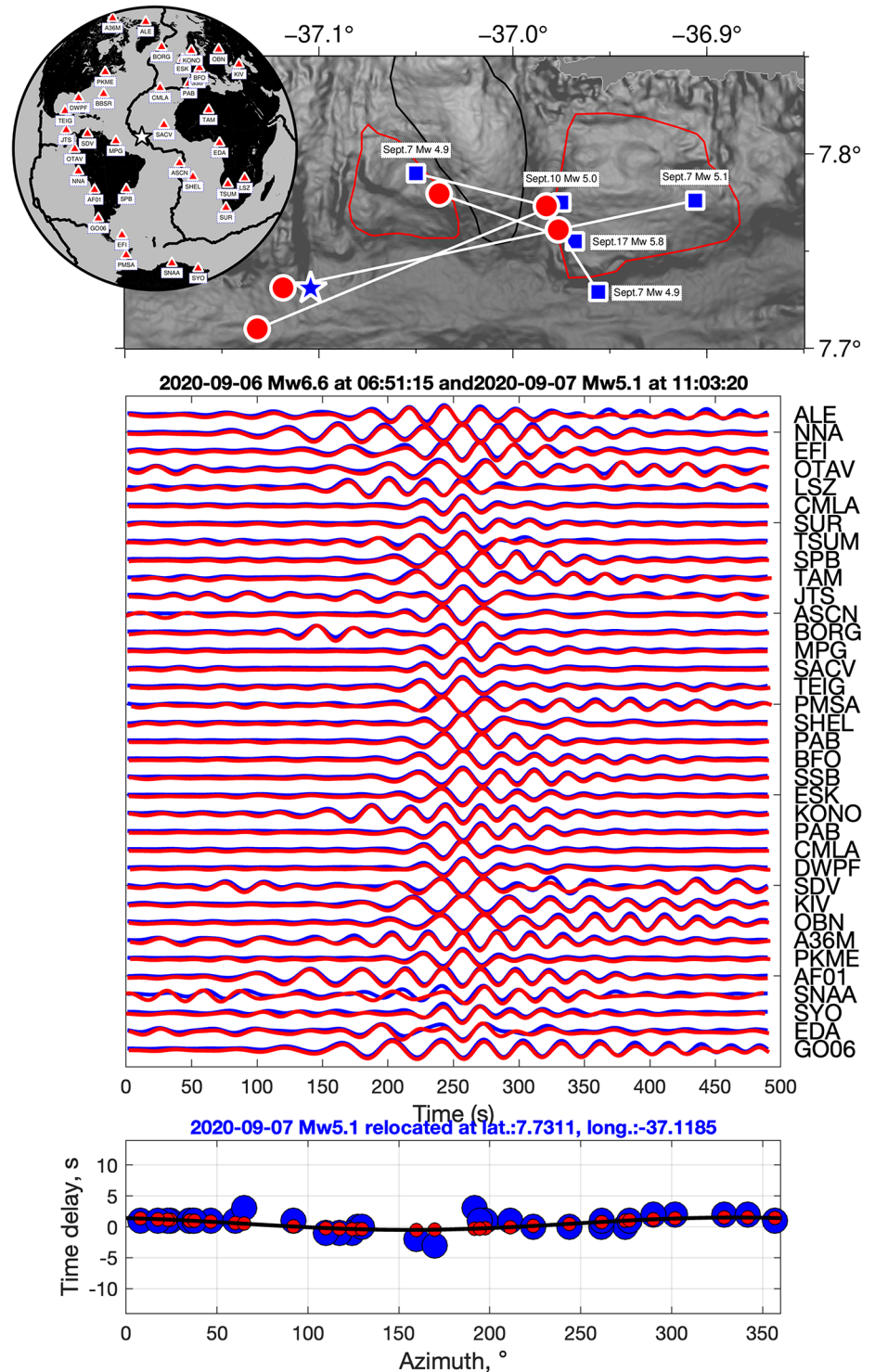
Discussion

The Mw 6.6 Vernadsky transform valley earthquake has been located within 4.8 km of the PTDZ (Fig. 5a), with aftershocks relatively relocated near to section B of the 7.78º OCC. The earthquake swarm was confined mostly to the region north and east of the Mw 6.6 event, with no events to the west, implying an asymmetric response to stress changes following the mainshock. We seek to explain these features below by constraining the extent of the first rupture and gain insight by modelling associated Coulomb stress changes.

Table 1 Our estimations of the new epicenter obtained by relative relocation for earthquakes Mw > 5.9, using teleseismic surface wave records. We include the separation distance between the mainshock (master) and relocated epicenter of the other five paired earthquakes

Date (MM DD, YYYY)	Magnitude (Mw_GCMT)	Origin time (HYPO71 location)	Lat. (º) (relatively relocated)	Long. (º) (relatively relocated)	Distance (km)
Sep. 7, 2020	5.1	11:03:20	7.7310	-37.1185	0.6±2.9
Sep. 7, 2020	4.9	21:19:05	7.7732	-36.9827	14.2±1.5
Sep. 7, 2020	4.9	21:22:46	7.7609	-36.9766	14.5±1.5
Sep. 10, 2020	5.0	22:26:40	7.710	-37.1318	3.8±1.7
Sep. 17, 2020	5.8	03:00:23	7.7745	-37.0430	8.3±1.2

Table 2 Focal depths obtained in this study

Date (MM DD, YYYY)	Magnitude (Mw_GCMT)	Depth (km)	Centroid time (relative to origin time)	Station
Sep. 6, 2020	6.6	6.0±2	+ 1.2 s	NBMO, SACV, MPG, SMTB, SOK, ITTB
Sep. 17, 2020	5.8	8.0±2	+0.4 s	NBMO, SACV, MPG, SMTB, SOK, ITTB

Rupture length of the Mw 6.6 event

Strong oceanic transform earthquakes produce ruptures that enlarge rapidly in horizontal extent with increasing moment magnitude (Boettcher and Jordan 2004). Rupture areas have been estimated based on aftershock distributions (Roland and McGuire 2009; McGuire et al. 2012). From the W-E extent of epicenters (Fig. 5d), the rupture likely extended for ~ 26–30 km. Although some earthquakes rupture asymmetrically (Scholz

Fig. 8 Synthetic waveform fitting of observed waveforms (black) to resolve focal depth of the mainshock Mw 6.6. Gray waveforms show the model obtained with the focal depth (6 km) that produces the best fit

DC: 100% (fixed)
Centroid time: +1.2 s
Centroid depth: 6±2 km
Mw 6.54±0.12
Moment: 8.17e+18
Variance: 0.52
Condition number: 9.0
Nodal plane 1: 273˚/89˚/-173˚
Nodal plane 2: 183˚/83˚/-1˚
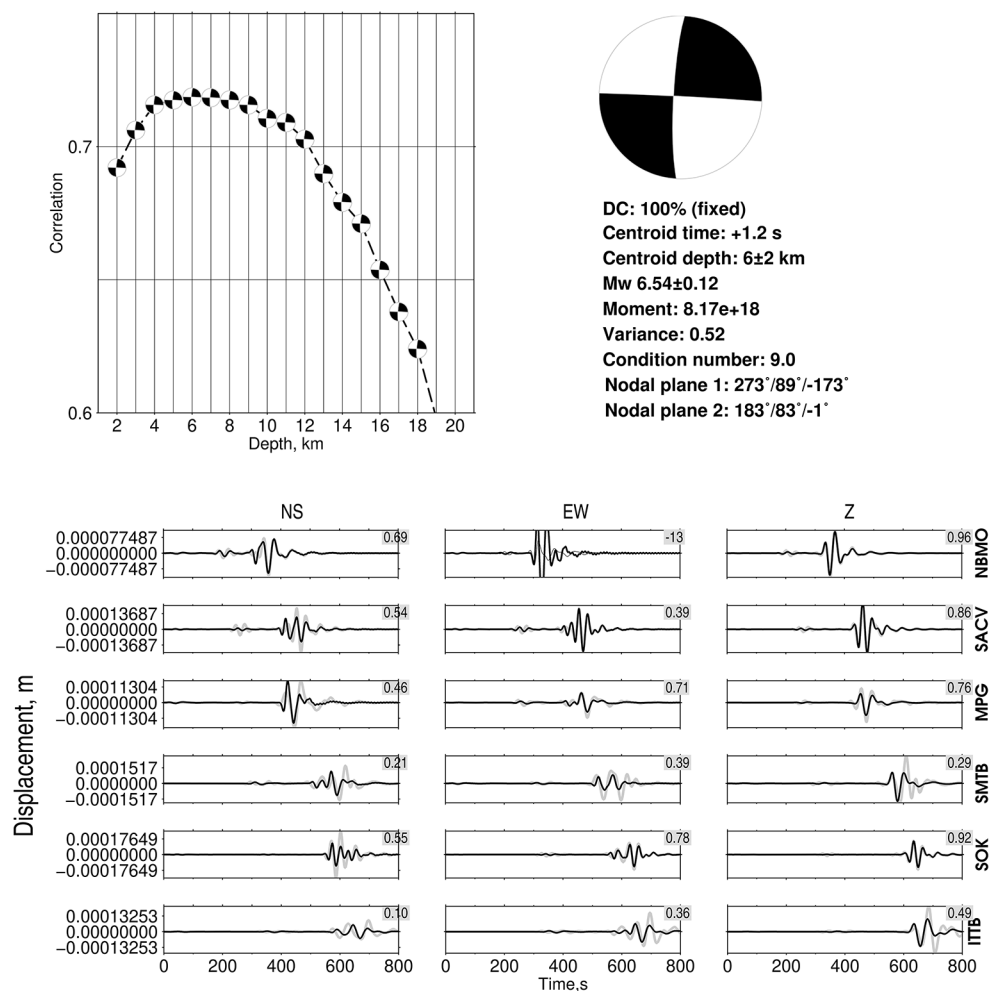
2019), the lack of seismicity to the west of the main shock suggests that this rupture length is an under-estimate if the fault ruptured more symmetrically about the epicenter (low-magnitude aftershocks to the west may have remained undetected). Wells and Coppersmith (1994) produced an empirical relationship for the fault rupture lengths of strike-slip earthquakes (Fig. 9). Our 26–30 km rupture length overlaps with the 31.5 km length predicted by the Wells and Coppersmith (1994) relationship. Source time function (STF) analysis of the SCARDEC database (Vallée and Douet 2016; http://scardec.projects.sismo.ipgp.fr/) shows that the transform fault movement lasted ~9s during the event. If we assume an average oceanic rupture velocity of 3.0–4.5 km/s (Abercrombie and Ekström 2001), the SFT event duration suggests a rupture length of ~37–40.5 km. Results obtained from hydroacoustic records suggest that the transform ruptured eastward ~50±8 km during the Mw 6.6 event (de Melo et al. 2024b). These various estimates suggest that our 26–30 km aftershock-based rupture length may be an under-estimate, compared with several other oceanic transform faults (Fig. 9) presenting rupture lengths higher than the relationship of Wells and Coppersmith (1994).

Coulomb stress changes during of the Mw 6.6 earthquake and their relationship to the aftershocks

During an earthquake, two types of stresses are generated: dynamic stress, which occurs during the propagation of seismic waves, and static stress, which is the general coseismic impact in the local epicentral region along the fault displacement created by the earthquake (Jin and Fialko 2020). The static stress changes was modeled using the Coulomb3 package (Toda et al. 2011), which predicts the static changes in Coulomb stress resulting from fault slips. Results are sensitive to model assumptions, hypocenter and faulting geometry (Harris and Simpson 2002).

For a single fault, Coulomb fault stress change $\Delta CFS = \Delta \tau_{shear} + \mu (\Delta \tau_n + \Delta P)$, where $\Delta \tau_{shear}$ is the shear stress change along the slip direction, μ is the static friction coefficient, $\Delta \tau_n$ is the normal stress change across the fault plane, and ΔP is the change in pore pressure at the fault (Byerlee 1978; Jaeger et al. 2009). Δ signifies moderate changes in these quantities. If pore pressures around the fault increase due to compaction, effective stress decreases and may cause a fault to slip. Serpentinites can deform non-dilatantly, thus leading to increased pore pressures further promoting deformation (Escartin et al. 1997). Additionally, if CFS is reduced due to thermo-chemical alteration, such as serpentinization, this will also favor slip. Typically, μ values of basaltic rocks are 0.59–0.78 (Giacomel et al. 2021). Serpentinite rocks have been found in the transform valley walls on the west side of the Vernadsky transform valley (Skolotnev et al. 2020). We, therefore, ran the model with physical properties appropriate for serpentinities. Serpentinites have a friction coefficients of ~0.3 (Escartin et al. 1997; Reinen et al. 1994) and Poisson's

Fig. 9 Empirical relationship between rupture length and moment magnitude. Red curve is the relationship of Wells and Coppersmith (1994). Vertical brown line shows the rupture length estimate for the Mw6.6 event based on the aftershock distribution. Also shown are estimates for one strong earthquake (2016 Mw 7.1) on the Romanche transform fault (Bao et al. 2022; Hicks et al. 2020), three earthquakes (1967 Ms 6.5; 1974 Ms 6.9; 2015 Mw 7.1) in the Charlie-Gibbs transform system (Kanamori and Stewart 1976; Aderhold and Abercrombie 2016), and one event (2003 Mw 6.2) in the Oceanographer transform fault (Pro et al. 2007)
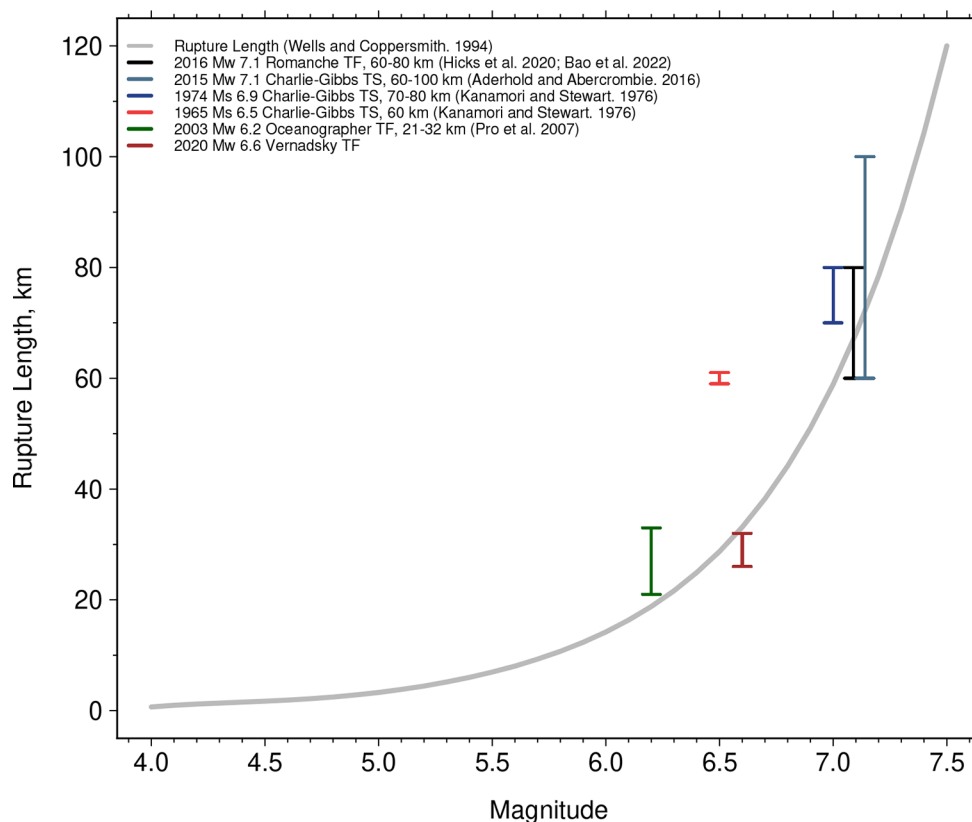
ratios of 0.25–0.35, depending on volume percent of olivine alteration (Christensen 2004). We estimated ΔCFS using a friction coefficient of 0.3, assuming a focal depth below seabed of 6 km (from the Mw 6.6-event waveform modelling). We assume a rupture from seabed to 12 km depth, i.e., symmetrical about the earthquake focus (Fig. S19 shows the grid used in modeling in plan view; Fig. S20 shows other model examples using 8 and 10 km). A 31.5 km rupture length from the Wells and Coppersmith (1994) relation was used. The lateral extent of inelastic movement (fault zone) was set to 1 km either side of each fault ("normal" abyssal hills near to the PTDZ appear undeformed (see immediately NW of the Mw 6.6 epicenter in Fig. 5a), suggesting that earthquakes generally do not shear the adjacent lithosphere). Young's modulus of 6.5×10^4 MPa was used. Coulomb stress changes caused by both the Mw 6.6 and Mw 5.8 events were predicted using the same strike/dip/slip

parameters as used in focal depth analysis (Section "Relative relocation of the aftershocks M>4.5"). To check the calculations, static Coulomb stress changes were modeled also using the DIS3D code of Fialko and Rubin (1999) with similar parameters (Fig. S21).

The Coulomb stress changes predicted for the Mw 6.6 event (Fig. 10a) are negative where most of the aftershocks occurred up until the Mw 5.8 aftershock, in contrast with models for other strike-slip earthquakes, which predict aftershocks in areas of positive change (King et al. 1994). In the model including the further effects of the Mw 5.8 aftershock, some of the area that had positive stress change from the mainshock (36.8–36.9ºW, 7.7ºN, Fig. 10a) also become negative (Fig. 10b). The aftershocks occurring after the Mw 5.8 event lay in the north walls and floor of the transform valley in areas of both positive and negative stress, though
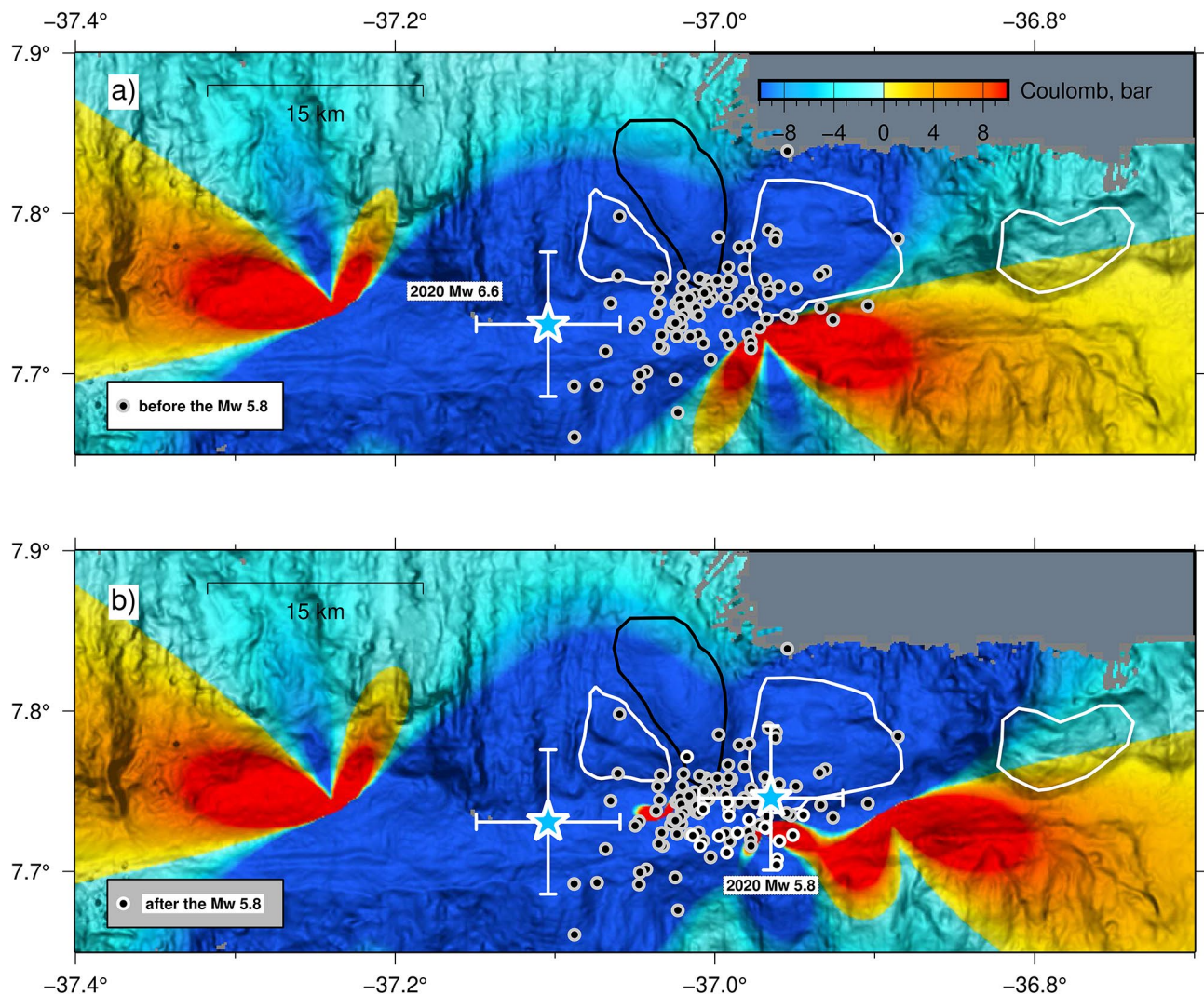

Fig. 10 Coulomb stress changes (see main text for model parameters). (a) Effect of the Mw 6.6 mainshock. (b) Effect of the Mw 5.8 aftershock in addition to the Mw 6.6 mainshock. Solid circles in both panels are the aftershocks relocated using HYPODD. Those occurring before the Mw 5.8 aftershock have grey outlines, those occurring after it have white outlines

mostly near their boundary, similar to the Hector Mine earthquake.

Although unexpected (King et al. 1994), aftershocks in areas of negative Coulomb stresses have been identified for some continental strike-slip earthquakes. For example, the 1968 Borrego Mountain earthquake (magnitude 6.4) caused slip of the San Andreas transform where a negative static Coulomb was expected (Allen et al. 1972). Several events of the 1999 Hector Mine sequence occurred in areas of negative Coulomb stress change generated by the M 7.2 1992 Landers earthquake (Toda et al. 2005; Freed 2005). The Hector Mine hypocenter was located near the border between positive and negative stress changes (Freed 2005; Harris and Simpson 2002). Stresses change during the propagation of earthquakes (called dynamic stresses). Although lasting only seconds, dynamic stresses are an order of magnitude larger than static Coulomb stress changes and have been suggested to cause aftershocks for many months following major earthquakes, by somehow modifying fault properties (Kilb et al. 2000).

A few features of the lithosphere encompassing the Vernadsky aftershocks are also noteworthy. During rapid compression of rock during seismic wave propagation, pore waters become compressed causing increased pore fluid pressure and decreased effective stresses. If serpentinites underlie the OCC segment B and other areas, this may be especially relevant given the low permeability of serpentinite and tendency for non-dilatant failure (Escartín et al. 2001). Furthermore, geological models of OCC development suggest that the upper crust and mantle in these areas could be highly heterogenous lithologically (Escartín et al. 2017) and serpentinization may be limited to the upper 5 km (Minshull et al. 1998). We therefore speculate that stress concentration or spatially varied damage from dynamic stresses may be possible, ultimately revealed by aftershocks occuring in areas of reduced Coulomb stresses.

Conclusion

Earthquake recordings from regional seismic data have been used to relocate aftershocks associated with the Mw 6.6 Vernadsky earthquake (a strike-slip event). From waveform modeling, the earthquake occurred 6 km below seafloor. Based on the aftershock distribution, the rupture length extended over 26-30 km, which is shorter than other estimates from teleseismic or hydroacoustic methods. This suggests that rupture lengths of oceanic transform fault earthquakes may be poorly estimated from such low-magnitude earthquakes recorded at regional distances. Better rupture constraints are provided by other records (e.g. hydroacoustic signals).

The Mw 6.6 mainshock was located only 4.8 km north of an E-W ridge within the transform valley, which likely represents the principal transform displacement zone (a geological constraint). The relocated aftershocks occur both along the transform valley floor and over an oceanic core complex in its north wall. Three aftershocks (including the Mw 5.8 aftershock) were relatively relocated by cross-correlation of surface waves. Those relocated epicenters lie close to the oceanic core complex.

Aftershocks for continental strike-slip earthquakes typically occur where long-term static Coulomb stresses increase, but numerical modeling here suggests that the aftershocks of the Mw 6.6 mainshock occurred in areas of decreased stress. The later Mw 5.8 event caused further modest Coulomb stress changes and some aftershocks occurred at boundaries between positive and negative changes.

Previous studies have shown that even with negative static stress, the dynamic stress generated by the earthquakes can modify the strength of local faults. Most of these aftershocks seem to have been generated by such dynamic stress modifications of fault strengths. Modification of pore pressure by the mainshock may have modified the rocks strength locally (e.g. serpentinite), reactivating preexisting faults around the OCC. Future more detailed local studies with ocean bottom seismometers or hydrophone arrays, if rapidly deployed after events like the Mw 6.6 mainshock, could help us to improve understanding of the dynamic behavior of lithosphere surrounding them.

Declarations

Competing interests The authors declare no competing interests.

References

Abercrombie RE, Ekström G (2001) Earthquake slip on oceanic transform faults. Nature 410(6824):74–77. https://doi.org/10.1038/35065064

Aderhold K, Abercrombie RE (2016) The 2015 mw 7.1 earthquake on the Charlie-Gibbs transform fault: repeating earthquakes and multimodal slip on a slow oceanic transform. Geophys Res Lett 43(12):6119–6128. https://doi.org/10.1002/2016GL068802

Allen CR, Wyss M, Brune JN, Grantz A, Wallace RE (1972) Displacements on the Imperial, Superstition Hills, and San Andreas faults triggered by the Borrego Mountain earthquake. US Geol Surv Prof Pap 787:87–104

Bao H, Xu L, Meng L, Ampuero JP, Gao L, Zhang H (2022) Global frequency of oceanic and continental supershear earthquakes. Nat Geosci 15(11):942–949. https://doi.org/10.1038/s41561-022-01055-5

Bianchi MB, Assumpção M, Rocha MP, Carvalho JM, Azevedo PA, Fontes SL, Costa IS (2018) The Brazilian seismographic network (RSBR): improving seismic monitoring in Brazil. Seismol Res Lett 89(2A):452–457. https://doi.org/10.1785/0220170227

Blackman DK, Cann JR, Janssen B, Smith DK (1998) Origin of extensional core complexes: evidence from the Mid-atlantic Ridge at Atlantis fracture zone. J Geophys Research: Solid Earth 103(B9):21315–21333. https://doi.org/10.1029/98JB01756

Blackman DK, Karson JA, Kelley DS, Cann JR, Früh-Green GL, Gee JS, Williams EA (2002) Geology of the Atlantis Massif (Mid-atlantic Ridge, 30 N): implications for the evolution of an ultramafic oceanic core complex. Mar Geophys Res 23(5):443–469. https://doi.org/10.1023/B:MARI.0000018232.14085.75

Blackman DK, Karner GD, Searle RC (2008) Three-dimensional structure of oceanic core complexes: Effects on gravity signature and ridge flank morphology, Mid-Atlantic Ridge, 30 N. Geochem Geophys Geosyst 9(6). https://doi.org/10.1029/2008GC001951

Boettcher MS, Jordan TH (2004) Earthquake scaling relations for mid-ocean ridge transform faults. J Geophys Research: Solid Earth 109(B12). https://doi.org/10.1029/2004JB003110

Bonnemains D, Escartín J, Mével C, Andreani M, Verlaguet A (2017) Pervasive silicification and hanging wall overplating along the 13° 20′ N oceanic detachment fault (M id-A tlantic R idge). Geochem Geophys Geosyst 18(6):2028–2053. https://doi.org/10.1002/2017GC006846

Byerlee J (1978) Friction of rocks. Rock friction and earthquake prediction. Birkhäuser, Basel, pp 615–626. https://doi.org/10.1007/978-3-0348-7182-2

Cann JR, Blackman DK, Smith DK, McAllister E, Janssen B, Mello S, Escartin J (1997) Corrugated slip surfaces formed at ridge–transform intersections on the Mid-atlantic Ridge. Nature 385(6614):329–332. https://doi.org/10.1038/385329a0

Christensen NI (2004) Serpentinites, peridotites, and seismology. Int Geol Rev 46(9):795–816. https://doi.org/10.2747/0020-6814.46.9.795

Cleveland KM, Ammon CJ, Kintner J (2018) Relocation of light and moderate-magnitude (M4–6) seismicity along the central Mid-Atlantic. Geochem Geophys Geosyst 19(8):2843–2856. https://doi.org/10.1029/2018GC007573

Collins JA, Smith DK, McGuire JJ (2012) Seismicity of the Atlantis Massif detachment fault, 30° N at the Mid-atlantic Ridge. Geochem Geophys Geosyst, 13(10). https://doi.org/10.1029/2012GC004210

Craig TJ, Parnell-Turner R (2017) Depth-varying seismogenesis on an oceanic detachment fault at 13° 20′ N on the Mid-atlantic Ridge. Earth Planet Sci Lett 479:60–70. https://doi.org/10.1016/j.epsl.2017.09.020

de Melo GWS, Mitchell NC, Zahradnik J, Dias F, do Nascimento AF (2021) Oceanic seismotectonics from regional earthquake recordings: the 4–5° N mid-atlantic ridge. Tectonophysics 819:229063. https://doi.org/10.1016/j.tecto.2021.229063

de Melo GWS, Mitchell NC, Zahradnik J Corrigendum to Oceanic seismotectonics from regional earthquake recordings: The 4–5° N Mid-Atlantic Ridge[de Melo, Mitchell GW, Zahradnik NC, Dias J, F.,do, Nascimento AF (2024a) (2021). Tectonophysics, 819, 229063]. *Tectonophysics*, *871*, 230157. https://doi.org/10.1016/j.tecto.2023.230157

de Melo GWS, Grevemeyer I, Metz D, Lange D, Kopp H (2024b) Rupture behavior of large strike-slip earthquakes at Equatorial Atlantic Oceanic Transform Faults: constraints from Hydroacoustic Data. SSA Annual Meeting 2024. https://doi.org/10.1785/0220240136. Abstract

DeMets C, Gordon RG, Argus DF (2010) Geologically current plate motions. Geophys J Int 181(1):1–80

Dziewonski AM, Chou TA, Woodhouse JH (1981) Determination of earthquake source parameters from waveform data for studies of global and regional seismicity. J Geophys Research: Solid Earth 86(B4):2825–2852. https://doi.org/10.1029/JB086iB04p02825

Ekström G, Nettles M, Dziewoński AM (2012) The global CMT project 2004–2010: Centroid-moment tensors for 13,017 earthquakes. Phys Earth Planet Inter 200:1–9. https://doi.org/10.1016/j.pepi.2012.04.002

Escartin J, Hirth G, Evans B (1997) Effects of serpentinization on the lithospheric strength and the style of normal faulting at slow-spreading ridges. Earth Planet Sci Lett 151(3–4):181–189. https://doi.org/10.1016/S0012-821X(97)81847-X

Escartin J, Hirth G, Evans B (2001) Strength of slightly serpentinized peridotites: implications for the tectonics of oceanic lithosphere. Geology 29(11):1023–1026. https://doi.org/10.1130/0091-7613(2001)029%3C1023:SOSSPI%3E2.0.CO;2

Escartin J, Mevel C, Petersen S, Bonnemains D, Cannat M, Andreani M et al (2017) Tectonic structure, evolution, and the nature of oceanic core complexes and their detachment fault zones (13 20′ N and 13 30′ N, Mid Atlantic Ridge). Geochem Geophys Geosyst 18(4):1451–1482. https://doi.org/10.1002/2016GC006775

Fialko YA, Rubin AM (1999) What controls the along-strike slopes of volcanic rift zones? J Geophys Research: Solid Earth 104(B9):20007–20020. https://doi.org/10.1029/1999JB900143

Freed AM (2005) Earthquake triggering by static, dynamic, and post-seismic stress transfer. Annu Rev Earth Planet Sci 33(1):335–367. https://doi.org/10.1146/annurev.earth.33.092203.122505

Giacomel P, Ruggieri R, Scuderi MM, Spagnuolo E, Di Toro G, Collettini C (2021) Frictional properties of basalt experimental faults and implications for volcano-tectonic settings and geo-energy sites. Tectonophysics 811:228883. https://doi.org/10.1016/j.tecto.2021.228883

Grevemeyer I, Reston TJ, Moeller S (2013) Microseismicity of the Mid-atlantic Ridge at 7° S–8° 15′ S and at the Logatchev Massif oceanic core complex at 14° 40′ N–14° 50′ N. Geochem Geophys Geosyst 14(9):3532–3554. https://doi.org/10.1002/ggge.20197

Hanka W, Saul J, Weber B, Becker J, Harjadi P (2010) Real-time earthquake monitoring for tsunami warning in the Indian Ocean and beyond. Nat Hazards Earth Syst Sci 10(12):2611–2622. https://doi.org/10.5194/nhess-10-2611-2010

Harris RA, Simpson RW (2002) The 1999 M w 7.1 Hector Mine, California, earthquake: a test of the stress shadow hypothesis? Bull Seismol Soc Am 92(4):1497–1512. https://doi.org/10.1785/0120000913

Henig AS, Blackman DK, Harding AJ, Canales JP, Kent GM (2012) Downward continued multichannel seismic refraction analysis of Atlantis Massif oceanic core complex, 30 N, Mid-Atlantic Ridge. Geochem Geophys Geosyst 13(5). https://doi.org/10.1029/2012GC004059

Hicks SP, Okuwaki R, Steinberg A, Rychert CA, Harmon N, Abercrombie RE, Sudhaus H (2020) Back-propagating supershear rupture in the 2016 M w 7.1 Romanche transform fault earthquake. Nat Geosci 13(9):647–653. https://doi.org/10.1038/s41561-020-0619-9

Horning G, Sohn RA, Canales JP, Dunn RA (2017) Local seismicity of the rainbow massif on the Mid-atlantic Ridge. J Geophys Research: Solid Earth 123(2):1615–1630. https://doi.org/10.1002/2017JB015288

Howe M, Ekström G, Nettles M (2019) Improving relative earthquake locations using surface-wave source corrections. Geophys J Int 219(1):297–312. https://doi.org/10.1093/gji/ggz291

Ivanova EV, Skolotnev SG, Borisov DG, Demidov AN, Bich AS, Gippius FN, Sholukhov KN (2020) Multidisciplinary investigation of the Transform Fault zones Doldrums and Vema during Cruise 45 of the R/V Akademik Nikolaj Strakhov. Oceanology 60(3):424–426. https://doi.org/10.1134/S0001437020030029

Jaeger JC, Cook NG, Zimmerman R (2009) Fundamentals of rock mechanics. Wiley

Jin Z, Fialko Y (2020) Finite slip models of the 2019 Ridgecrest earthquake sequence constrained by space geodetic data and aftershock locations. Bull Seismol Soc Am 110(4):1660–1679. https://doi.org/10.1785/0120200060

Kanamori H, Stewart GS (1976) Mode of the strain release along the Gibbs fracture zone, Mid-Atlantic Ridge. Phys Earth and Planet inter 11(4):312–332. https://doi.org/10.1016/0031-9201(76)90018-2

Kilb D, Gomberg J, Bodin P (2000) Earthquake triggering by dynamic stresses. Nature 408:570–574. https://doi.org/10.1007/978-0-387-30440-3_157

Kim WY, de Melo GWS, Assumpcao M (2024) A pn magnitude scale mb (pn) for earthquakes along the equatorial Mid-atlantic Ridge. Geophys J Int ggae242. https://doi.org/10.1093/gji/ggae242

King GC, Stein RS, Lin J (1994) Static stress changes and the triggering of earthquakes. Bull Seismol Soc Am 84(3):935–953. https://doi.org/10.1785/BSSA0840030935

Laske G, Masters G, Ma Z, Pasyanos M (2013, April) Update on CRUST1. 0—A 1-degree global model of Earth's crust. Geophysical research abstracts, vol 15. EGU General Assembly, Vienna, Austria, p 2658. 15

Lee WHK, Valdes CM (1985) HYPO71PC: a personal computer version of the HYPO71 earthquake location program, vol 85. No. 749). US Geological Survey. https://doi.org/10.3133/ofr85749

Mallows C, Searle RC (2012) A geophysical study of oceanic core complexes and surrounding terrain, Mid-atlantic Ridge 13° N–14° N. Geochem Geophys Geosyst, 13(6). https://doi.org/10.1029/2012GC004075

Matias L, Dias NA, Morais I, Vales D, Carrilho F, Madeira J, Silveira AB (2007) The 9th of July 1998 Faial Island (Azores, North Atlantic) seismic sequence. J Seismolog 11:275–298. https://doi.org/10.1007/s10950-007-9052-4

McGuire JJ (2008) Seismic cycles and earthquake predictability on East Pacific Rise transform faults. Bull Seismol Soc Am 98(3):1067–1084. https://doi.org/10.1785/0120070154

McGuire JJ, Collins JA, Gouédard P, Roland E, Lizarralde D, Boettcher MS, Van Der Hilst RD (2012) Variations in earthquake rupture properties along the Gofar transform fault, East Pacific rise. Nat Geosci 5(5):336–341. https://doi.org/10.1038/ngeo1454

Minshull TA, Muller MR, Robinson CJ, White RS, Bickle MJ (1998) Is the oceanic Moho a serpentinization front? In: Mills RA and K (ed) Harrison (editors), modern ocean floor processes and the geological record. Geological Society, London, London, pp 71–80

Pan J, Dziewonski AM (2005) Comparison of mid-oceanic earthquake epicentral differences of travel time, centroid locations, and those determined by autonomous underwater hydrophone arrays. J Geophys Research: Solid Earth 110(B7). https://doi.org/10.1029/2003JB002785

Parnell-Turner R, Sohn RA, Peirce C, Reston TJ, MacLeod CJ, Searle RC, Simão NM (2017) Oceanic detachment faults generate compression in extension. Geology 45(10):923–926. https://doi.org/10.1130/G39232.1

Parnell-Turner R, Sohn RA, Peirce C, Reston TJ, MacLeod CJ, Searle RC, Simão NM (2021) Seismicity trends and detachment fault structure at 13° N, Mid-atlantic Ridge. Geology 49(3):320–324. https://doi.org/10.1130/G48420.1

Peyve AA, Sokolov SY, Ivanenko AN, Razumovskiy AA, Patina IS, Bogolubskiy VA, Veklich IA, Denisova AP, Dobrolyubov VN, Dokashenko SA, Ivanova ES, Lapina SA, Naumov IA, Nikitin NS, Urazmuratova ZF (2022, December) Accretion of the oceanic crust in the Mid-Atlantic Ridge (48°–51.5° N) during "dry" spreading. In: Doklady earth sciences, Vol. 507, No. Suppl 3. Moscow: Pleiades Publishing, pp. S349–S356. https://doi.org/10.1134/S1028334X226014442

Pro C, Buforn E, Udías A (2007) Rupture length and velocity for earthquakes in the Mid-Atlantic Ridge from 2 directivity effect in body and surface waves. Tectonophysics 433(1–4):65–79. https://doi.org/10.1016/j.tecto.2006.12.011

Reinen LA, Weeks JD, Tullis TE (1994) The frictional behavior of lizardite and antigorite serpentinites: experiments, constitutive models, and implications for natural faults. Pure appl Geophys 143(1):317–358. https://doi.org/10.1007/BF00874334

Roland E, McGuire JJ (2009) Earthquake swarms on transform faults. Geophys J Int 178(3):1677–1690. https://doi.org/10.1111/j.1365-246X.2009.04214.x

Rollins JC, Stein RS (2010) Coulomb stress interactions among M ≥ 5.9 earthquakes in the Gorda deformation zone and on the Mendocino Fault Zone, Cascadia subduction zone, and northern

San Andreas Fault. J Geophys Research: Solid Earth 115(B12). https://doi.org/10.1029/2009JB007117

Romanowicz B, Cara M, Fel JF, Rouland D (1984) GEOSCOPE: a French initiative in long-period three-component global seismic networks. Eos Trans Am Geophys Union 65(42):753–753. https://doi.org/10.1029/EO065i042p00753-01

Ryan WB, Carbotte SM, Coplan JO, O'Hara S, Melkonian A, Arko R, Weissel RA, Ferrini V, Goodwillie A, Nitsche F, Zemsky R (2009) Global multi-resolution topography synthesis. Geochem Geophys Geosyst 10(3). https://doi.org/10.1029/2008GC002332

Sandwell DT, Müller RD, Smith WH, Garcia E, Francis R (2014) New global marine gravity model from CryoSat-2 and Jason-1 reveals buried tectonic structure. Science 346(6205):65–67. https://doi.org/10.1126/science.1258213

Sautter B, Escartin J, Petersen S, Gaina C, Granot R, Pubellier M (2024) MAPRIDGES: global database of Mid-Oceanic ridges segments and transform faults. SEANOE. https://doi.org/10.17882/99981

Schlindwein V, Schmid F (2016) Mid-ocean ridge seismicity reveals extreme types of ocean lithosphere. Nature 535:276–279. https://doi.org/10.1038/nature18277

Scholz CH (2019) The mechanics of earthquakes and faulting. Cambridge University Press. https://doi.org/10.1017/9781316681473

Scripps Institution of Oceanography (1986) IRIS/IDA seismic network. *International Federation of Digital Seismograph Networks*

Searle R (2013) Mid-ocean ridges. Cambridge University Press, New York, p 318. https://doi.org/10.1017/CBO9781139084260

Searle RC, Cowie PA, Mitchell NC, Allerton S, MacLeod CJ, Escartin J, Russell SM, Slootweg PA, Tanaka T (1998) Fault structure and detailed evolution of a slow spreading ridge segment: the Mid-atlantic Ridge at 29˚N. Earth Planet Sci Lett 154:167–183. https://doi.org/10.1016/S0012-821X(97)00160-X

Seton M, Müller RD, Zahirovic S, Williams S, Wright NM, Cannon J, Whittaker JM, Matthews KJ, McGirr R (2020) A global data set of present-day oceanic crustal age and seafloor spreading parameters. Geochem Geophys Geosyst 21(10):e2020GC009214. https://doi.org/10.1029/2020GC009214

Skolotnev SG, Sanfilippo A, Peyve AA, Muccini F, Sokolov SY, Sani C, Ligi M (2020) Large-scale structure of the Doldrums multi-fault transform system (7–8ºN equatorial Atlantic): preliminary results from the 45th expedition of the R/V AN Strakhov. Ofioliti 45(1):25–41. https://doi.org/10.4454/ofioliti.v45i1.553

Smith DK, Cann JR, Escartín J (2006) Widespread active detachment faulting and core complex formation near 13 N on the Mid-atlantic Ridge. Nature 442(7101):440–443. https://doi.org/10.1038/nature04950

Smith DK, Escartín J, Schouten H, Cann JR (2008) Fault rotation and core complex formation: Significant processes in seafloor formation at slow-spreading mid-ocean ridges (Mid-Atlantic Ridge, 13–15 N). Geochem Geophys Geosyst 9(3). https://doi.org/10.1029/2007GC001699

Smith DK, Schouten H, Dick HJ, Cann JR, Salters V, Marschall HR, Curry S (2014) Development and evolution of detachment faulting along 50 km of the Mid-atlantic Ridge near 16.5° N. Geochem Geophys Geosyst 15(12):4692–4711. https://doi.org/10.1002/2014GC005563

Sokos EN, Zahradnik J (2008) ISOLA a Fortran code and a Matlab GUI to perform multiple-point source inversion of seismic data. Comput Geosci 34(8):967–977. https://doi.org/10.1016/j.cageo.2007.07.005

Toda S, Stein RS, Richards-Dinger K, Bozkurt SB (2005) Forecasting the evolution of seismicity in southern California: animations built on earthquake stress transfer. J Geophys Research: Solid Earth 110(B5). https://doi.org/10.1029/2004JB003415

Toda S, Stein RS, Sevilgen V, Lin J (2011) Coulomb 3.3 Graphic-rich deformation and stress-change software for earthquake, tectonic, and volcano research and teaching—user guide. *US Geological Survey open-file report*, *1060*(2011), 63

Vallée M, Douet V (2016) A new database of source time functions (STFs) extracted from the SCARDEC method. Phys Earth Planet Inter 257:149–157. https://doi.org/10.1016/j.pepi.2016.05.012

Waldhauser F, Ellsworth WL (2000) A double-difference earthquake location algorithm: Method and application to the northern Hayward fault, California. Bull Seismol Soc Am 90(6):1353–1368. https://doi.org/10.1785/0120000006

Waldhauser F, Schaff D (2007) Regional and teleseismic double-difference earthquake relocation using waveform cross-correlation and global bulletin data. J Geophys Research: Solid Earth 112(B12). https://doi.org/10.1029/2007JB004938

Wells DL, Coppersmith KJ (1994) New empirical relationships among magnitude, rupture length, rupture width, rupture area, and surface displacement. Bull Seismol Soc Am 84(4):974–1002. https://doi.org/10.1785/BSSA0840040974

Wessel P, Luis JF, Uieda L, Scharroo R, Wobbe F, Smith WH, Tian D (2019) The generic mapping tools version 6. Geochem Geophys Geosyst 20(11):5556–5564. https://doi.org/10.1029/2019GC008515

Zahradník J, Sokos E (2018) ISOLA code for multiple-point source modeling. *Moment tensor solutions: A useful tool for seismotectonics*, 1–28. https://doi.org/10.1007/978-3-319-77359-9_1

Terms and Conditions

Springer Nature journal content, brought to you courtesy of Springer Nature Customer Service Center GmbH ("Springer Nature").

Springer Nature supports a reasonable amount of sharing of research papers by authors, subscribers and authorised users ("Users"), for small-scale personal, non-commercial use provided that all copyright, trade and service marks and other proprietary notices are maintained. By accessing, sharing, receiving or otherwise using the Springer Nature journal content you agree to these terms of use ("Terms"). For these purposes, Springer Nature considers academic use (by researchers and students) to be non-commercial.

These Terms are supplementary and will apply in addition to any applicable website terms and conditions, a relevant site licence or a personal subscription. These Terms will prevail over any conflict or ambiguity with regards to the relevant terms, a site licence or a personal subscription (to the extent of the conflict or ambiguity only). For Creative Commons-licensed articles, the terms of the Creative Commons license used will apply.

We collect and use personal data to provide access to the Springer Nature journal content. We may also use these personal data internally within ResearchGate and Springer Nature and as agreed share it, in an anonymised way, for purposes of tracking, analysis and reporting. We will not otherwise disclose your personal data outside the ResearchGate or the Springer Nature group of companies unless we have your permission as detailed in the Privacy Policy.

While Users may use the Springer Nature journal content for small scale, personal non-commercial use, it is important to note that Users may not:

1. use such content for the purpose of providing other users with access on a regular or large scale basis or as a means to circumvent access control;

2. use such content where to do so would be considered a criminal or statutory offence in any jurisdiction, or gives rise to civil liability, or is otherwise unlawful;

3. falsely or misleadingly imply or suggest endorsement, approval , sponsorship, or association unless explicitly agreed to by Springer Nature in writing;

4. use bots or other automated methods to access the content or redirect messages

5. override any security feature or exclusionary protocol; or

6. share the content in order to create substitute for Springer Nature products or services or a systematic database of Springer Nature journal content.

In line with the restriction against commercial use, Springer Nature does not permit the creation of a product or service that creates revenue, royalties, rent or income from our content or its inclusion as part of a paid for service or for other commercial gain. Springer Nature journal content cannot be used for inter-library loans and librarians may not upload Springer Nature journal content on a large scale into their, or any other, institutional repository.

These terms of use are reviewed regularly and may be amended at any time. Springer Nature is not obligated to publish any information or content on this website and may remove it or features or functionality at our sole discretion, at any time with or without notice. Springer Nature may revoke this licence to you at any time and remove access to any copies of the Springer Nature journal content which have been saved.

To the fullest extent permitted by law, Springer Nature makes no warranties, representations or guarantees to Users, either express or implied with respect to the Springer nature journal content and all parties disclaim and waive any implied warranties or warranties imposed by law, including merchantability or fitness for any particular purpose.

Please note that these rights do not automatically extend to content, data or other material published by Springer Nature that may be licensed from third parties.

If you would like to use or distribute our Springer Nature journal content to a wider audience or on a regular basis or in any other manner not expressly permitted by these Terms, please contact Springer Nature at

onlineservice@springernature.com